Mechanical and in situ thermal-related behavior during directed energy deposition additive manufacturing of a high-performance Al alloy

OPEN ACCESS
IMMT | IOP Publishing
International Journal of Extreme Manufacturing
Int. J. Extrem. Manuf. **8** (2026) 035002 (15pp)
https://doi.org/10.1088/2631-7990/ae3349

Mechanical and in situ thermal-related behavior during directed energy deposition additive manufacturing of a high-performance Al alloy

Da Guo[1,2,*], Chengbo Zhu[3], Harry E. Chapman[1,2], Kai Zhang[1,4], Wei Li[1,2], Shishira Bhagavath[1,2], Robert Atwood[5], Stefan Michalik[5], Dmitry G. Eskin[3], Iakovos Tzanakis[6], Chu Lun Alex Leung[1,2,*] and Peter. D. Lee[1,2,*]

[1] UCL Mechanical Engineering, University College London, London WC1E 7JE, United Kingdom
[2] Research Complex at Harwell, Harwell Campus, Didcot OX11 0FA, United Kingdom
[3] Brunel Centre for Advance Solidification Technology (BCAST), Brunel University of London, London UB8 3PH, United Kingdom
[4] School of Electrical, Electronic and Mechanical Engineering, University of Bristol, Bristol BS8 1TR, United Kingdom
[5] Diamond Light Source, Harwell Science and Innovation Campus, Didcot OX11 0DE, United Kingdom
[6] School of Engineering, Computing and Mathematics, Oxford Brookes University, Oxford OX33 1HX, United Kingdom

E-mail: da.guo@ucl.ac.uk, alex.leung@ucl.ac.uk and peter.lee@ucl.ac.uk

Received 17 June 2025, revised 6 September 2025
Accepted for publication 4 January 2026
Published 30 January 2026

Abstract

Directed energy deposition (DED) additive manufacturing (AM) can fabricate, repair, and join near-net-shaped components for high-performance engineering applications, including biomedical, energy, and transport sectors. The broader adoption of DED remains constrained by the limited number of alloys available that can be reliably manufactured without imperfections, hence limiting mechanical properties. Here, we designed an Al–Ni–Ce–Mn–Fe AM alloy that can achieve an ultra-fine microstructure (<5 μm), uniform distribution of intermetallics, low residual stress (<32 MPa), and superior mechanical properties in as-built DED components. Compared to DED AlSi10Mg in the as-built state using the same conditions, the yield increased by 70%, and the ultimate tensile strength by 50%. DED-AM involves rapid cooling and complex thermal conditions, which largely influence the property of the final components. Post-characterization cannot capture the time resolved thermal behavior, hence offer limited mechanism-based guide for alloy design. In this study, we develop a novel multimodal characterization methodology for correlative in situ X-ray imaging, X-ray diffraction, and

* Authors to whom any correspondence should be addressed.

infrared imaging, enabling quantification of the in situ thermal-related behavior, including phase evolution, temperature distribution, and stress accumulation during DED. We elucidated key mechanisms driving the structure refinement and stress development in this alloy. The insights gained into the interplay between alloy composition, thermal-related behavior, and performance under specific AM conditions inform next-generation material design tailored for AM technologies.

Supplementary material for this article is available online

Keywords: directed energy deposition, synchrotron X-ray diffraction, synchrotron X-ray imaging, microstructure, properties, additive manufacturing

1. Introduction

Additive manufacturing (AM) technologies enable layer-by-layer fabrication of high-performance metallic components for biomedical, energy, and transport applications, with unparalleled benefits, such as increased shape complexity and reduced waste[1]. The current development of the AM industry focuses on process optimization, with less attention being paid to alloy design[2,3]. The quality of the AM parts largely depends on the properties of the alloy feedstock; however, current commercial alloys were designed based on traditional processes with cooling rates of 2–4 orders of magnitude slower than experienced in directed energy deposition (DED) AM, and 4–6 orders of magnitude slower than laser powder bed fusion (LPBF) AM[4].

Aluminum (Al) alloys are widely used as a structural material due to their excellent strength-to-weight ratio and corrosion resistance. The most studied Al-materials in AM are near eutectic Al-Si alloys, such as AlSi10Mg[5], which are usually crack-free and high-density (>99%)[6] but exhibit a relatively low tensile strength (<200 MPa). There is a strong demand for high-performance AM Al-alloys with low crack susceptibility, good strength, and high thermal stability. One approach is adding alloying elements with low diffusivity and solubility (e.g. transition metals and rare earth elements with near eutectic compositions), reducing the freezing range[7,8]. In comparison to Al-Si, alloys including Al–Sc–Zr (Scalmalloy®)[9], Al-Fe-Zr (Constellium Aheadd® CP1)[10,11], additions of nanoparticles[12–14], and near eutectic Al-alloys with additions of Fe, Ni, Mn, and/or Ce[15–17] have been tried mainly for LPBF. They have had varied success in producing improved mechanical properties and density (>99%) with minimal cracks; though, these alloys usually require heat treatment or the addition of grain refiners to achieve desirable properties. DED-AM offers key advantages over LPBF, including the ability to fabricate large components and perform repairs; however, the alloy design methodology for DED-AM remains largely unexplored.

To achieve ultrafine grain size and enhanced mechanical properties, we designed a hypereutectic Al alloy within the Al–Ni–Ce–Mn–Fe system (denoted as PA1), optimized to promote the formation of primary intermetallic phases. The chemical compositions of PA1 are detailed in the **Methods** section. The rapid cooling conditions during DED are expected to substantially refine the intermetallic and grain size, thereby improving the alloy's overall performance. The DED-AM process of this alloy offers an ideal testbed for investigating the influence of in situ thermal-related behavior on its final properties. Synchrotron X-ray source is widely used for advanced in situ characterization in either real space (imaging)[18–20] or reciprocal space (diffraction)[21–23]. Here, we establish a novel multimodal characterization methodology that integrates in situ X-ray imaging, X-ray diffraction, and infrared imaging (IR) for material design purposes. This approach enables precise quantification of phase evolution, thermal profiles, and stress accumulation during DED, and holds a significant promise for guiding the design of next-generation metallic materials tailored for high-temperature, rapid solidification manufacturing processes.

2. Methods

2.1. Materials

The feedstock material was a bespoke aluminum alloy (PA1) powder produced by Amazemet (Warsaw, Poland) through ultrasonic atomization based on Al–Ni–Ce–Mn–Fe alloy system, with the chemical composition given in Table 1. The designed Al alloy aims to achieve low cracking susceptibility and high thermal stability. The deterioration of the strength of Al alloys at high temperatures is generally due to the dissolution of constitutive phases, precipitates, and grain coarsening[24]. To counter those effects, alloying elements with low diffusivity and solubility in the Al were selected, i.e., Ce, Fe, Mn, and Ni. Ce was selected as it can, by forming a eutectic, improve fluidity in the melt and form intermetallics that resist grain coarsening[25]. As Fe is an inevitable impurity in Al, a minor content of Fe, 0.3 wt%, was added to the alloy. Mn and Ni possess the potential to improve the strength in an Al-RE system through forming thermally stable phases[26].

The powder morphology (see Figure 1(a)) and size distribution (see Figure S1) were characterized using scanning electron microscopy (SEM) with 5 kV (JEOL JSM-6610 LV, Japan). The substrates were produced by EDS cutting from cast ingots of the same composition.

Table 1. Chemical composition of PA1 alloy (wt%).

Elements	Al	Mn	Ni	Ce	Fe	Zr
PA1	Bal	1.84	5.5	4.6	0.3	0.3

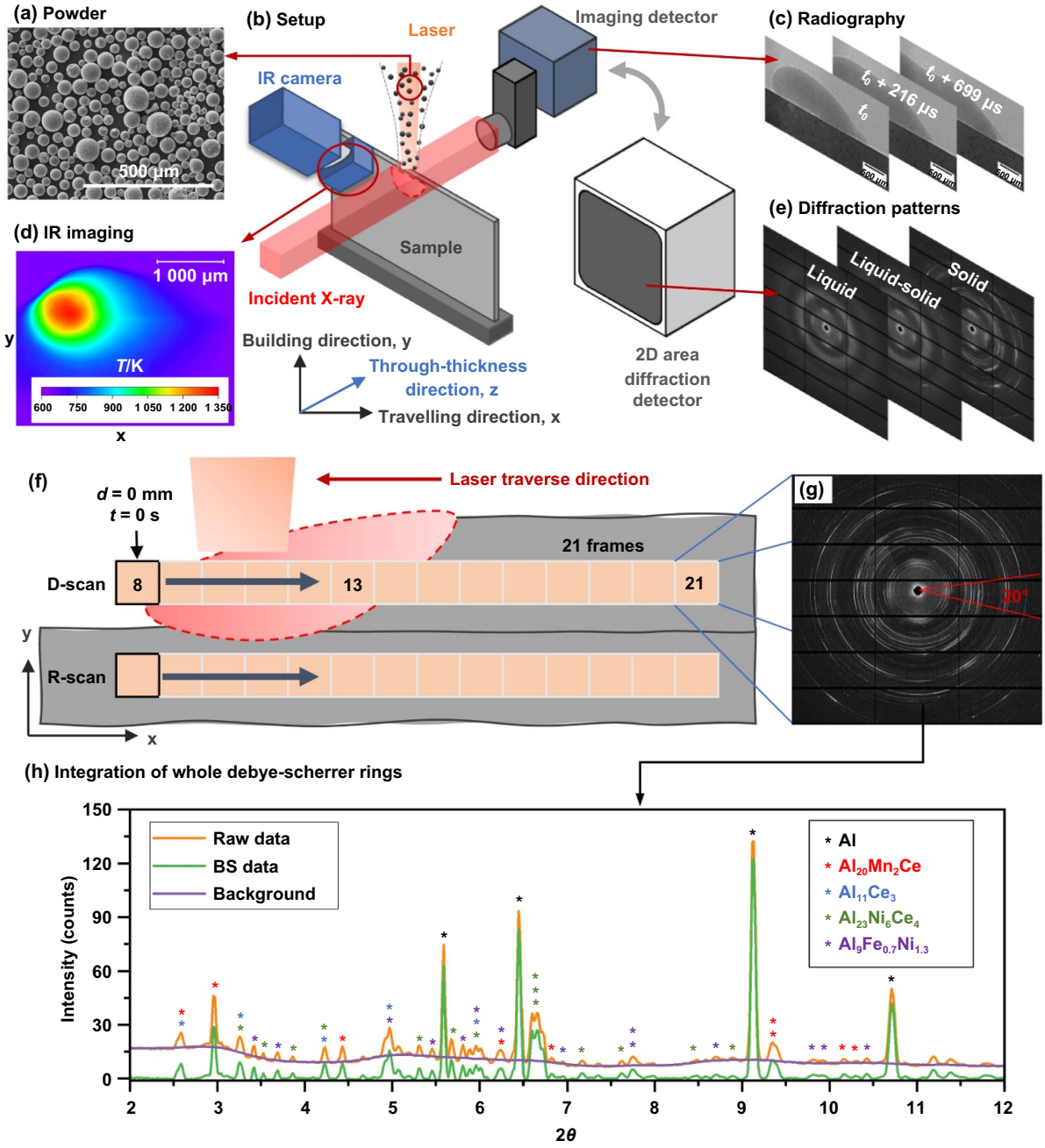

Figure 1. Schematic of experimental set up during DED aluminum and data processing: (a) powder morphology of aluminum alloy PA1, (b) set up of correlative in situ X-ray imaging, IR imaging and X-ray diffraction, with representative results demonstrated in (c), (d) and (e) respectively, (f) scan strategy of in situ X-ray diffraction with (g) one frame of diffraction pattern at full solid state and (h) 2D profile of intensity as a function of 2-theta after integration.

2.2. DED process replicator

The experiments were performed using a bespoke DED process replicator, called the Blown Powder Additive Manufacturing Process Replicator, 2nd Generation (BAMPRII)[27]. The BAMPRII rig comprised a continuous wave (CW) 1 070 nm Ytterbium-doped fiber laser with laser power up to 200 W (SPI Lasers Ltd, UK) coaxially through a blown powder nozzle, combined with a custom-built environmental chamber with an argon atmosphere.

Prior to each experiment, a substrate with a dimension of 60 mm × 20 mm × 1.5 mm was mounted on the triaxial sample stage (Aerotech, US). The powder was delivered from the industrial powder feeder (Oerlikon Metco TWIN-10-C, Switzerland) to the nozzle via an argon carrier gas feedline. The coaxial laser beam melted the incoming powder and the substrate to mimic the DED process. A laser power of 200 W, spot size of 400 μm, scan speed of 2 mm·s^{-1} and powder feed rate of 10% RPM were used for thin plate samples during in situ experiments. For larger block samples (12 layers, dimension: 15 mm × 15 mm × 5 mm), a laser of 350 W, spot size of 400 μm, scan speed of 4 mm·s^{-1}, powder feed rate of 10% RPM, and hatching distance of 0.35 mm were used. The larger layer thickness and reduced cooling rate resulting from the lower scan speed in the in situ study provided stronger diffraction signals and more detailed insights into the microstructure and thermal dynamics. Parameter optimization for block samples was carried out to achieve high density while minimizing defect formation.

2.3. Correlative infrared (IR) imaging, X-ray imaging, and diffraction measurements

The in situ experiments were carried out on the I12: Joint Engineering, Environmental, and Processing (JEEP) beamline[28] at the Diamond Light Source under the proposal number: MG-34549 (see experimental setup in Figure 1(b)). For high-speed X-ray imaging, a monochromatic X-ray beam with a fixed energy of ∼55 keV was used during the beamtime. The incident X-ray penetrated through the sample and the glassy carbon windows of the chamber during the DED process. The attenuated X-ray was converted by a scintillator that emitted visible light. Then the visible light image was magnified by 4× and then captured by a MIRO 310M camera with module 3 optics at a frame rate of 1 000 Hz (see Figure 1(c)). The field of view (FoV) was 7.6 × 3.2 mm with a pixel size of 6.67 μm. Before each experiment, 100 frames of flat field images were recorded. For each sample, 5 layers were built with a track length of 6 mm.

During the steady state deposition, an in situ DED diffraction experiment was performed in transmission mode using the same X-ray energy and printing conditions with X-ray imaging. Meanwhile, the thermal imaging was captured through an FLIR X6900sc camera at a frame rate of 1 000 Hz, at a 40° angle to the X-ray beam path (see Figure 1(d)). The camera is equipped with a macro lens, resulting in a pixel size of 32.7 μm. A standard LaB_6 sample was used for calibration prior to the main DED experiments. The diffracted X-ray was captured through a large 2D area diffraction detector (Pilatus 2M CdTe), giving a FoV of 253.7 × 288.8 mm with a pixel size of 172 μm × 172 μm (see Figure 1(e)). The sample-detector distance was selected as approximately 560 mm to capture 5 Al reflections: (1 1 1), (2 0 0), (2 2 0), (3 1 1), and (2 2 2). A stationary laser with a moving substrate mimicked the DED process, while keeping the melt pool stationary with respect to the replicator. 21 frames were scanned on the depositing layer or underlying layer for each experiment during deposition by moving the replicator across the X-ray beam path. This scanned the beam across the steady state melt pool and allowed the diffraction frames to cover the phase transition from liquid to solid state and subsequent re-heating events, as illustrated in Figure 1(f). The framerate used in the in situ diffraction mode was 10 Hz with an exposure time of ∼0.095 s. An X-ray beam size of 200 × 200 μm was employed during all the experiments. Three diffraction scan modes were used, see details in Figure S2. In mode 1 (D-scan), the 21 frames of diffraction patterns were taken on the top depositing layers (D1-D5), while in mode 2 (R-scan), the diffraction patterns were captured on Layer 1 while depositing subsequent Layers 2 to 5 to investigate the re-heating effect, denoted as R2-R5. Mode 3 (L-scan) is the post scan on the final product along the building direction in the center of each layer (L1–L5).

2.4. IR imaging calibration

The melt pool boundary temperature was taken as the liquidus temperature, which was calculated as 949 K from Thermo-Calc (see Figure S3) and used for IR calibration. The comparison between X-ray radiography and IR data is given in Figure S4. The solid emissivity was set as 0.15 after IR calibration, matching the emissivity range characterized for the solid Al alloy at high temperatures[29]. The emissivity value of Al is not expected to change drastically with temperature change[30]. For comparative analysis of the IR and X-ray diffraction data, the diffraction scanning path was determined via X-ray radiography during the in situ experiments. Subsequently, the diffraction scanning region was correlated with the IR-derived temperature field by matching the melt pool locations observed in the X-ray radiographs and IR measurements (see Figure S4).

2.5. Diffraction data processing

The collected 2D X-ray diffraction patterns (Figure 1(g)) were azimuthally integrated into 1D profiles (Figure 1(h)) to get the intensity as a function of Bragg's angle 2θ using DAWN® software[31,32]. The background was estimated through replacement of the intensity of k^{th} point by averaging its $2N$ neighbours via[33]:

$$I_k = \frac{1}{2N\sum_{j=-N}^{N} I_{k+j}} \tag{1}$$

where N spans over 2 to 4 times the full width at half maximum (FWHM) of Bragg peaks. The background estimation was iterated 20 times. After background subtraction, each Bragg peak of the background-subtracted (BS) data was fitted individually with Pseudo-Voigt function with bespoke MATLAB® scripts, see Figure S5, and compared with standard powder diffraction databases. Four phases have been identified, including intermetallic $Al_{11}Ce_3$, $Al_{23}Ni_6Ce_4$, $Al_{20}Mn_2Ce$, and $Al_9Fe_{0.7}Ni_{1.3}$ on a post-build sample.

2.5.1. Phase volume fraction calculation. Phase volume fractions were determined based on the integrated intensity of Bragg peaks, which can be expressed as[34,35]:

$$I_{hkl}^{\alpha}=\left[\frac{I_0\lambda^3}{32\pi r}\frac{e_c^4}{m_e^2c^4}\right]\left[\frac{p\left(hkl\right)}{2V_{\alpha}^2}\left|F_{(hkl)}^2\right|\right.$$
$$\left.\times\left(\frac{1+cos^2 2\theta cos^2 2\theta_m}{sin^2\theta cos\theta}\right)\right]\left[\frac{W_{\alpha}}{\rho_{\alpha}\mu_m^*}\right], \quad (2)$$

where I_{hkl}^{α} is the integrated intensity of reflection (hkl) for phase α, I_0 is the incident X-ray beam intensity, λ is the wavelength, r is the detector-electron distance, e_c is the electron charge, m_e is the electron mass, c is the speed of light, $p\left(hkl\right)$ is the multiplicity, V_{α} is the volume of unite cell, F_{hkl} is the structure factor, θ is half of the Bragg angle, θ_m is the monochromator angle, taken as 0 for transmission X-ray diffraction. W_{α} is the weight fraction, ρ_{α} is the density, and μ_m^* is the mass absorption coefficient. For each intermetallic phase, the integrated intensity of highest-intensity peak was used for quantification. Equation (2) can be simplified to the relative integrated intensity, I_{hkl}^R as:

$$I_{hkl}^R=p_{hkl}\left|F_{hkl}^2\right|\frac{1+\cos^2 2\theta}{\cos\theta\sin^2\theta}A\left(\theta\right)e^{-2M_T}, \quad (3)$$

where $A\left(\theta\right)$ equals $1/\mu_m^*$, describing the diffraction angle dependent absorption constant, and e^{-2M_T} is the Debye temperature factor.

The phase volume fraction ϕ_{α} of phase α is equal to the W_{α}/ρ_{α} in Equation (2). Combining Equations (2) and (3), the experimentally measured integrated intensity, I_{hkl}^{α} can be expressed as:

$$I_{hkl}^{\alpha}=I_s p_{hkl}\left|F_{hkl}^2\right|\frac{1+\cos^2 2\theta}{\cos\theta\sin^2\theta}e^{-2M_T}\phi_{\alpha}, \quad (4)$$

where I_s is the scaling factor, describing all the unknown constants in Equation (2), and it can be calculated assuming the sum of volume fractions for all the phases equals 1. I_{hkl}^{α} can be calculated directly from the fitted data, and p_{hkl} for each reflection of different phases is listed in Table 2. The structure factor, F_{hkl} is given as:

$$F_{hkl}=\sum f_j e^{\left[-2\pi i\left(hx_j+ky_j+lz_j\right)\right]}, \quad (5)$$

where f_j is the atomic scattering factor for each element, which can be determined via:

$$f=\sum_{i=1}^{4}a_i\exp\left(-\frac{b_i sin^2\theta}{\lambda^2}\right)+c, \quad (6)$$

where a_i, b_i, and c can be found in[36]. x_j, y_j and z_j are the atom coordinates listed in Table 2. The temperature factor for each phase can be yielded through multiple reflections (the selected reflections (hkl) are listed in Table 2), which is detailed in[34].

2.5.2. Temperature and stress calculation. The deformation of a Debye Scherrer ring comes from both (1) uniform expansion due to increased temperature and (2) anisotropic mechanical stress applied on the measured volume. To separate the temperature and stress effect, the whole Debye Scherrer rings were segmented into 18 regions with $\Delta\psi=20°$ (see Figure 1(g)) to covering the ψ range from $-180°$ to $180°$ before integration and fitting. $sin^2\psi$ method was used via the following formula[41]:

$$\varepsilon_{hkl}=\frac{d_{hkl}\left(T\right)-d_0\left(T\right)}{d_0\left(T\right)}=-\frac{1}{2}S_2\sigma sin^2\psi, \quad (7)$$

where $d_{hkl}\left(T\right)$ is the measured lattice spacing of reflection (hkl) at elevated temperature (T) during DED process, here data of reflections Al (1 1 1), Al (2 0 0), Al (2 2 0) and Al (3 1 1) were used. $d_0\left(T\right)$ is the temperature-dependant stress-free lattice spacing, $-\frac{1}{2}S_2$ is the X-ray elastic constant and σ is the in-plane stress. Equation (7) can be converted to $d_{hkl}=-\frac{1}{2}d_0 S_2\sigma sin^2\psi+d_0\left(T\right)$, and fitting the linear equation between a_{hkl} and $sin^2\psi$ enables to yield the y-intercept $d_0\left(T\right)$. The lattice parameter, a can be calculated through $a=d\sqrt{h^2+k^2+l^2}$.

The temperature-dependent lattice parameter can be estimated for pure Al through a phenomenological model[42], without the consideration of composition effects:

$$a_0\left(T\right)=a_{RT}\exp\left(A\left(T-T_{RT}\right)+\frac{B}{2}\left(T^2-T_{RT}^2\right)\right), \quad (8)$$

where $a_0\left(T\right)$ is the temperature-dependent stress-free lattice spacing, a_{RT} is the lattice parameter at room temperature, $T_{RT}=298$ K, which is calculated as 4.047 6. A and $\frac{B}{2}$ are 1.68×10^{-5} and 1.01×10^{-8}, respectively[42]. The temperature evolution can then be deduced from Equation (8) with calculated $a_0\left(T\right)$.

To calculate the biaxial principal stress state, the following equation[43] was used with an assumption that the through-thickness stress is 0 as the build sample thickness was negligible compared to width and height:

$$\varepsilon_{hkl}=p_{xx}\sigma_{xx}+p_{xy}\sigma_{xy}+p_{yy}\sigma_{yy}, \quad (9)$$

where p_{ij} are the lattice plane dependent stress factors and σ_{ij} are the 2D components macro-mechanical stress tensors. The stress factors can be expressed with X-ray elastic constant S_1^{hkl} and $\frac{1}{2}S_2^{hkl}$:

$$p_{xx}=S_1^{hkl}+\frac{1}{2}S_2^{hkl}cos^2\left(\psi\right), \quad (10.a)$$

$$p_{xy}=\frac{1}{2}S_2^{hkl}\sin\left(2\psi\right), \quad (10.b)$$

$$p_{yy}=S_1^{hkl}+\frac{1}{2}S_2^{hkl}sin^2\left(\psi\right). \quad (10.c)$$

The temperature-dependent elastic constant can be determined through the methods introduced in[44,45].

2.6. Microstructural characterization

For microstructural analysis, samples were cross-sectioned, mounted, ground, and polished to a 0.25 μm finish. The microstructure was analyzed using a TESCAN MAGNA Scanning Electron Microscope (SEM) equipped with a backscattered electron (BSE) detector and an Oxford Symmetry S3 Electron Backscatter Diffraction (EBSD) detector. AZtech & Channel 5

Table 2. Crystallographic information of different phases in DED PA1.

Phase	Space group	(*hkl*)-Multiplicity	Atom coordinates
Al	$Fm\bar{3}m$ (cubic)	(1 1 1)-12 (2 0 0)-6 (2 2 0)-12 (3 1 1)-24	Al: [0 0 0], [0 0.5 0.5], [0.5 0 0.5], [0.5 0.5 0]
$Al_{11}Ce_3$[37]	Immm (Orthorhombic)	(0 0 2)-2 (0 3 1)-4 (1 3 0)-4 (0 3 3)-4	Al: [0.5 0 0.5], [0 0.2181 0.5], [0 0.3683 0.3338], [0 0.2729 0.1378] Ce: [0 0 0], [0 0 0.31688]
$Al_{23}Ni_6Ce_4$[38]	C2/m (monoclinic)	(4 0 0)-2 (0 0 5)-2 (1 1 5)-4 (−7 1 5)-4 (−7 1 1)-4 (−8 0 1)-2	Al: [0 0 0], [0.4312 0 −0.4400], [0.1247 0.5 0.0956], [−0.0317 −0.5 −0.2826], [0.4177 −0.5 −0.1879], [0.2040 0 −0.9784], [−0.0899 0 −0.7778], [0.3565 −0.5 −0.3588], [−0.2220 −0.5 −0.8235], [−0.1075 0.5 −0.6591], [0.2548 0 −0.4549], [−0.0898 0 −0.5476] Ni: [0.30989 0 −0.56644], [−0.00741 0 −0.63292], [−0.22619 0 −0.89737] Ce: [0.26445 0 −0.28226], [0.57002 0 −0.09317]
$Al_{20}Mn_2Ce$[39]	$Fd\bar{3}m$ (cubic)	(2 2 0)-12 (3 1 1)-24 (4 2 2)-24 (10 2 2)-24 (9 5 3)-48	Al: [0 0 0], [0.4843 0.125 0.125], [0.0584 0.0584 0.3252], Mn: [0.5 0.5 0.5] Ce: [0.125 0.125 0.125]
$Al_9Fe_{0.7}Ni_{1.3}$[40]	$P2_1/c$ (monoclinic)	(1 1 1)-4 (0 1 2)-2 (−2 0 2)-2 (−1 2 2)-4	Al: [0 0 0], [0.0886 0.7106 0.2301], [0.2122 0.3875 0.0429], [0.4041 0.0287 0.2679], [0.6098 0.1950 0.0040] 0.35Fe +0.65Ni: [0.26434 0.3798 0.3333]

software was used for the processing and analysis of the EBSD data.

2.7. Profilometry-based Indentation Plastometry (PIP) testing

The tensile property of each alloy was evaluated by a profilometry-based indentation plastometry (PIP)[46] on the plane perpendicular to the building direction. During the test, PIP pushed an indenter made of WC-Co cermet of a radius of 1 mm into the sample with a known force, followed by the measurement of the indent profile. An iterative finite element method (FEM) was performed to fit the material's plasticity parameters with the indentation profile. When a best-fit set of the plasticity parameter values was obtained, it led to the true stress-strain relationship and the material's properties. The PIP technique offers a rapid and reliable means of estimating the tensile properties of metals. Its accuracy has been validated against conventional tensile testing across 12 alloys in[47]. More recently, this approach has been applied to additively manufactured components[48,49]. Moreover, PIP is well suited to specimens exhibiting inhomogeneity and anisotropy[49], and such capability is particularly valuable for DED-produced samples with columnar grains oriented along the build direction.

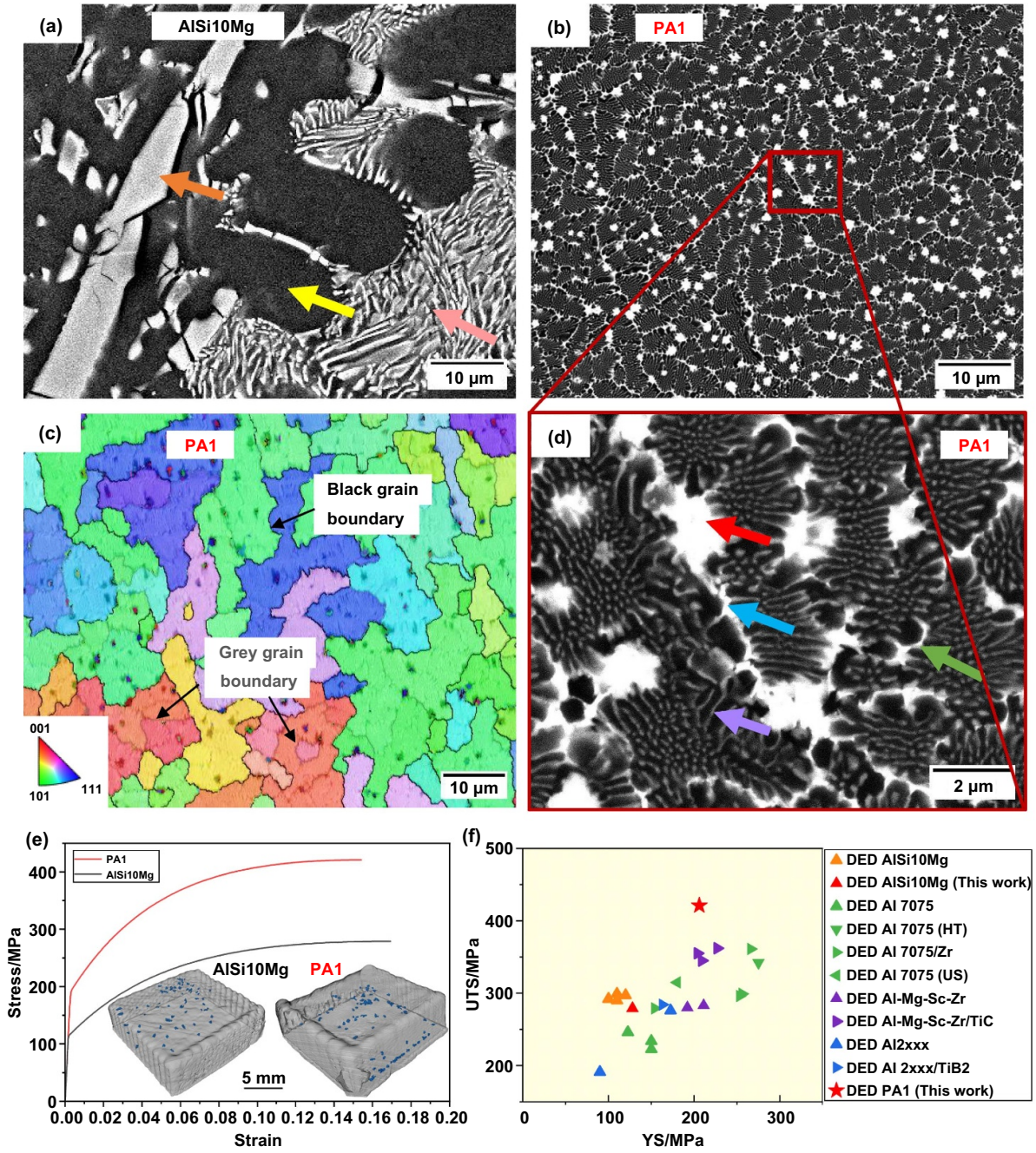

Figure 2. Microstructure and mechanical property of DED PA1 aluminum (block sample): (a) microstructure of DED AlSi10Mg, where the yellow arrow indicates α-Al dendrites, pink arrow indicates Al-Si eutectic, and orange arrow indicates faceted Si particles. (b) DED PA1. (c) EBSD of DED PA1 with a grain boundary. (d) Magnified region from (b), where the red arrow indicates $Al_{20}Mn_2Ce$, green arrow indicates $Al_{23}Ni_6Ce_4$, blue arrow indicates $Al_{11}Ce_3$, and purple arrow indicates $Al_9Fe_{0.7}Ni_{1.3}$. (e) Strain-stress curve upon PIP of DED block sample, and (f) comparison of mechanical properties between DED PA1 (PIP estimate) and other DED Al alloys[50–61].

3. Results and discussion

3.1. Microstructure and mechanical properties

Figure 2(a) reveals the microstructure of a reference as-built DED AlSi10Mg alloy, comprised of typical α-Al dendrites (yellow arrow), lamellar Al-Si eutectic (pink arrow), and large faceted Si particles (orange arrow) solidified under DED's non-equilibrium conditions. Figure 2(b) shows the microstructure of the developed DED PA1 alloy, and a SEM microstructure containing 5 layers is shown in Figure S6, where the interlayer region presents larger grains compared to the intralayer due to the re-heating effect. It exhibits a much finer eutectic structure with a sub-grain (eutectic colony) size of <5 μm in the as-built state and a uniform distribution of intermetallics, growing along the eutectic colony boundaries. The Electron Backscatter Diffraction (EBSD) analysis in Figure 2(c) confirmed the average (quasi-equiaxed) eutectic

grain size of ∼22.1 μm with high-angle (>10°) grain boundaries (black) and a sub-grain (eutectic colony) size of <5 μm marked by low-angle sub-grain boundaries (grey). The larger-scale EBSD and grain size distribution are detailed in Figure S7. Such a grain size is comparable to DED-fabricated Al 7075 with a grain refiner (average grain size of 22.7 μm[50]). In comparison, DED commercial Al alloys can have large columnar grains with a size >250 μm in the as-built state[50–52]. Five phases were identified in Figure 2(d), including star-shaped $Al_{20}Mn_2Ce$ (red arrow), $Al_{23}Ni_6Ce_4$ (blue arrow), and $Al_{11}Ce_3$ (green arrow) intermetallic phases along the sub-grain boundaries, and ultra-fine (∼0.2 μm spacing) lamellar Al-$Al_9Fe_{0.7}Ni_{1.3}$ eutectic (purple arrow). These phases were confirmed by synchrotron X-ray diffraction (sXRD) indexing in the **Methods** section and Scanning Electron Microscopy with Energy Dispersive X-ray (SEM-EDX) characterization in Figure S8.

Profilometry-based Indentation Plastometry (PIP) tests were conducted on DED printed block samples (15 × 15 × 5 mm) of both PA1 and AlSi10Mg alloys under the same printing conditions. The industry standard aluminum eutectic alloy for DED-AM is AlSi10Mg[53], therefore we've used this alloy as the baseline to compare with our alloy of the same structure (eutectic) type. Both as-built samples of PA1 and AlSi10Mg achieved a density of >99% (see the X-ray computed tomography scan and porosity distribution analysis in Figure S9). As illustrated in Figure 2(e), the as-built PA1 demonstrated a significantly increased yield strength (YS) of (191 ± 26) MPa and an ultimate tensile strength (UTS) of (421 ± 17) MPa, compared to (112 ± 16) MPa and (279 ± 21) MPa for AlSi10Mg. The PA1 alloy's improved properties can be attributed to the uniform distribution of high-strength intermetallics and the ultra-fine sizes of sub-grains (<5 μm) and eutectic lamellae (∼0.2 μm spacing). Compared to AlSi10Mg, the existence of the star-shaped $Al_{20}Mn_2Ce$ intermetallic can impede the movement of dislocations, improving the tensile properties via precipitation strengthening. The strengthening effect is well documented to be proportional to the volume fraction of precipitate and inversely proportional to precipitate size[62]. The intermetallic surrounding the sub-grain boundary will restrict sub-grain growth and dislocation movement, therefore, it has the similar effect to grain refinement strengthening. The contribution of grain refinement is also inversely proportional to grain size[62]. Therefore, the highly refined size and significant volume fraction of IMC will strengthen the alloy by both these mechanisms, as shown by the large increase in properties. In addition, the strength of the eutectic structure is dependent on the lamellar spacing, and the strengthening effect of fine lamellar is increased with decreased lamellar spacing[63].

However, the elongation of PA1 (15%) is slightly reduced compared to AlSi10Mg (17%), see Figure 2(e), most likely due to the presence of brittle intermetallics. The existence of small intermetallic particles in PA1 can be the nucleation site for micro-cracking during plastic deformation[64]. The volume fraction of intermetallics in PA1 (estimated by Thermocalc) is 16.15 vol%, while for AlSi10Mg it is 12 vol%. Therefore, although the strengthening mechanisms discussed raise the tensile strength of PA1, the ductility may be slightly reduced due to increased crack initiation by more numerous intermetallic phases. Figure 2(f) shows the comparison of the mechanical properties of DED PA1 with the reference data for other commonly used DED Al alloys. PA1 alloy exhibited a superior UTS over other DED printed Al alloys and had a comparable YS to DED samples with grain refiner or those that had undergone heat treatment (HT).

3.2. Microstructure evolution

The solidification path of PA1 alloy was evaluated using Scheil's equation with Thermo-calc (v. 2024b, database TCAL8), see Figure S3. In the calculation, $Al_{31}Mn_6Ni_2$, Al_4Mn, Al_6Mn, Al_3Ni, and $Al_{12}Mn$ were excluded because they were not observed in similar alloy systems[65]. The liquidus and solidus of the alloy were 949 K and 908 K, respectively. The solidification starts with a eutectic reaction with the formation of Al_8Mn_4Ce and $Al_{23}Ni_6Ce_4$, one of those may be formed as a primary phase due to the shift in the phase equilibria upon rapid solidification in DED. Subsequently, transitional and eutectic solidification reactions occur, leading to the formation of the $Al_9(Fe, Ni)_2$ and (Al) phases. The solidification ends with the formation of a complex eutectic comprised of all phases above.

To confirm the microstructural evolution sequence under non-equilibrium conditions during DED, we performed in situ sXRD during DED of PA1. Three sXRD scanning modes were used (see details in **Methods** and Figure S2), enabling in situ and ex situ monitoring of microstructure and stress formation, from deposition to re-heat to the final state. For the in situ scanning mode (a.k.a. D-scan), 21 frames across the melt pool to the solidified part were taken during the deposition of Layer 1 (D1) to cover the phase transformation from liquid to solid, see the integrated intensity evolution in Figure 3(a). The occurrence of $Al_{23}Ni_6Ce_4$ (green box) and $Al_{20}Mn_2Ce$ (red box) before the formation of Al (black box) indicates $Al_{23}Ni_6Ce_4$ and $Al_{20}Mn_2Ce$ are formed first. A similar scanning strategy was applied on Layer 1 during the deposition of subsequent layers on top, allowing investigation of re-heating effects, termed R-scans. Figure 3(b) gives the example of integrated intensity along 2-theta as a function of frames in Layer 1 during deposition of subsequence Layer 2 (R2). The melt pool is stationary with respect to the laser beam during deposition, see in situ X-ray imaging in Video S1, and the X-ray path was moved across the melt pool with Frame 8 located at the melt pool front (MPF), see inserted radiograph in Figure 3(c). The distance from the MPF (d) is set as 0 mm in Frame 8, respectively.

Figure 3(c) quantifies the phase fraction evolution in scan mode D1, where Frames 13–15 (1.0–1.4 mm from MPF) cover the mushy zone surrounding the liquid-solid boundary, with the liquid fraction dropping from 93.6% to 34.8%. Within these regions, the $Al_{23}Ni_6Ce_4$ and $Al_{20}Mn_2Ce$ (not included in the Thermocalc database and represented by Al_8CeM_4 in Figure S3) intermetallics initially formed at 1.0 mm from MPF, prior to the formation of the main eutectic containing

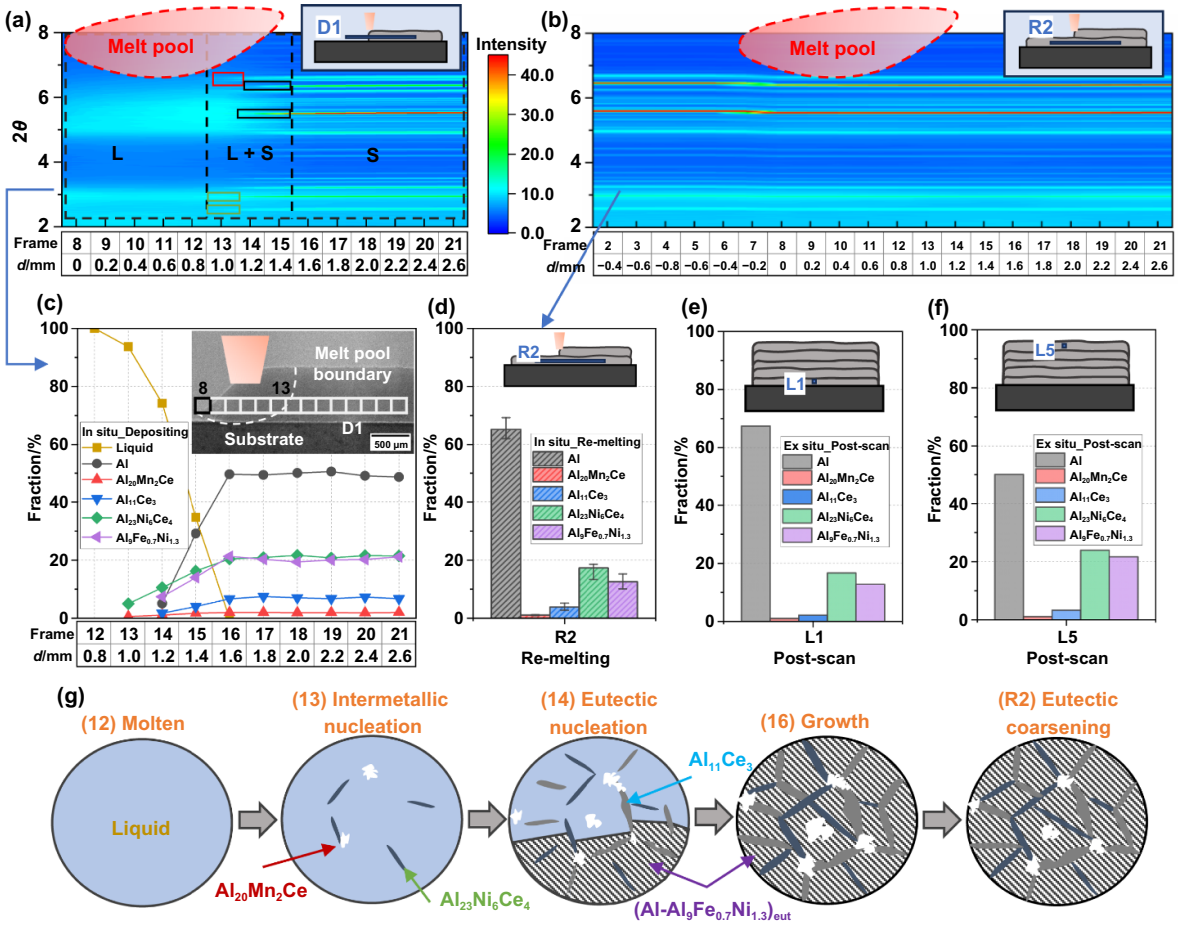

Figure 3. Microstructural evolution during DED PA1 alloy (plate sample): (a) phase evolution during deposition of Layer 1 (D1), shown as the integrated intensity along 2-theta vs. frames, indicating liquid (L), liquid and solid (L +S), and full solid (S) state. The green, red and black boxes indicate first appearance of $Al_{23}Ni_6Ce_4$, $Al_{20}Mn_2Ce$ and Al peak; (b) phase evolution of Layer 1 during deposition of subsequent Layer 2 (R2), shown as the integrated intensity along 2-theta vs. frames, (c) volume phase fraction evolution during deposition of Layer 1 (D1), (d) average volume phase fraction (21 frames) of Layer 1 during deposition of subsequence Layer 2 (R2), volume phase fraction (one frame) of (e) Layer 1 (L1) and (f) Layer 5 (L5) in post-build sample, and (g) schematic of microstructure refinement mechanism.

$Al_9Fe_{0.7}Ni_{1.3}$ (Al9M2 in Figure S3) and $Al_{11}Ce_3$ phases at 1.2 mm. The latter phase ($Al_{11}Ce_3$) was formed due to the highly nonequilibrium solidification conditions during DED and was not predicted by Thermocalc. The $Al_{11}Ce_3$ typically forms in alloys with Ce concentrations above 6 at.%[17], much higher than the concentration in PA1. However, Ce segregated at the boundaries due to its low solubility in both α-Al and $Al_9Fe_{0.7}Ni_{1.3}$[66]. The limited diffusion in the liquid under rapid cooling can promote local Ce segregation, leading to the formation of $Al_{11}Ce_3$ in these regions. The volume fraction of the eutectic $Al_9Fe_{0.7}Ni_{1.3}$ phase in the solidified part (after 1.6 mm from MPF) during deposition was ∼20%, compared to ∼22% of $Al_{23}Ni_6Ce_4$, ∼2% of $Al_{20}Mn_2Ce$, and ∼7% of $Al_{11}Ce_3$. Note that, although there is a broad agreement between the Thermocalc assessment in Figure S3 and the experimental data, some of the predicted phases may not form, or might form in quantities below the XRD detection limit, due to the nonequilibrium shift of phase equilibria and incomplete solidification reactions as a result of very high cooling rates during DED.

The re-heating effect of adding Layer 2 on the underlying Layer 1 (scan mode R2) resulted in coarsened eutectic and partially dissolved intermetallics, halving the amount of $Al_{20}Mn_2Ce$ and $Al_{11}Ce_3$ and reducing the $Al_{23}Ni_6Ce_4$ by ∼23%, as shown in the average phase fraction Figure 3(d). This indicated the nonequilibrium nature of these phases. During subsequent re-heating events (scan modes R3 to R5), there were minor changes in phase fractions (see Figure S10) in Layer 1 due to coarsening and equilibration during reheating. Since L2, L3, and L4 experienced sequentially reduced re-heating, their final phase fractions (see Figure S11) were similar to those in L1 (Figure 3(e)). In contrast, the top layer, L5, that did not undergo re-heating (Figure 3(f)), retained similar phase fractions to those seen in Layer 1 (scan mode D1) before subsequent reheating during depositions on top.

The microstructure refinement mechanism is illustrated in Figure 3(g). A prior study on cast Al-Ce-Mn alloy[67] suggested that the $Al_{20}Mn_2Ce$ and $Al_{10}Mn_2Ce$ formed from the onset of solidification prior to the formation of the eutectics. The addition of Ni to Al-Ce-Mn alloy resulted in the formation of the $Al_{23}Ni_6Ce_4$ intermetallic phase[68,69]. In PA1 alloy, the star-shaped $Al_{20}Mn_2Ce$ and short columnar-shaped $Al_{23}Ni_6Ce_4$ particles initially formed via a high-temperature

eutectic reaction, then grew, and were subsequently uniformly distributed in the molten matrix as divorced eutectic, making them appear like primary phases. Those divorced eutectic phases ($Al_{20}Mn_2Ce$ and $Al_{23}Ni_6Ce_4$) may restrain subsequent growth of more complex eutectics at lower temperature (Al+ $Al_{20}Mn_2Ce$+ $Al_{23}Ni_6Ce_4$+ $Al_{11}Ce_3$+ $Al_9Fe_{0.7}Ni_{1.3}$) during solidification, separating the eutectic grains into ultra-fine subgrains. The re-heating during deposition of subsequent layers might cause coarsening of some eutectic phases, while the final sub-structure size remained limited to ∼5 μm.

3.3. Temperature and thermal gradient evolution

The focused heat source in DED during deposition and re-heating effects of subsequent layers lead to complicated and evolving thermal conditions, which directly influence the microstructure and residual stress. Due to experimental limitations, most prior studies used thermo-mechanical simulations to try and understand the microstructure[70] and stress formation[71] mechanisms. Here, we use correlative in situ IR imaging and sXRD to obtain in-depth insights in the rapid solidification and stress accumulation during DED of PA1. This novel approach enabled experimental assessment of temperature gradients and thermal stresses through in situ monitoring the temperature distribution of the melt pool and its surroundings.

Isotherm lines in Figures 4(a)–(d) show the temperature distribution during the deposition of Layers 1 and 3, obtained through IR. The white dashed line indicates the melt pool boundary. The IR peak temperature within the melt pool was ∼1 350 K, which could be an underestimate as a constant solid emissivity was used, and the molten pool would have a much lower emissivity value. The color map in Figures 4(a) and (d) demonstrates the calculated thermal gradient in the two in-plane directions, G_x and G_y, during deposition of Layer 1 and 3. The average G_x and G_y along the melt pool boundary were (385 ± 255) K·mm^{-1} and (400 ± 233) K·mm^{-1} in Layer 1, compared to (299 ± 226) K·mm^{-1} and (351 ± 387) K·mm^{-1} in Layer 3. These values correlate well with prior work, being of the same magnitude as the liquidus thermal gradient of DED Al obtained through IR in reference[72] and mathematical simulation in reference[73]. Compared to Layer 1, the melt pool was slightly larger with a lower thermal gradient along the melt pool boundary in Layer 3. This was most likely due to the heat accumulation induced by subsequent layer deposition, leading to higher part temperatures and a more uniform thermal distribution.

For comparison, the temperature distribution determined from sXRD analysis using Al peaks is presented in Figure 4(e). During DED, we used bi-directional scanning, and hence we flipped the results for R2 and R4 horizontally for consistent visualization. The diffraction data provided the temperature of the solidified part. The solid region near the melt pool boundary (Frame 14, 1.2 mm from MPF) in scan mode D1 demonstrated a temperature near the solidus temperature of 882 K. The temperature continuously dropped to 712 K at 2.6 mm from MPF as the measured volume moved away from the laser beam. During the deposition of Layer 2, the temperature of Layer 1 (see R2 in Figure 4(e)) reached temperatures between 681 K and 717 K, resulting in significant coarsening and intermetallic dissolution (Figure 3(d)) compared to other subsequent re-heating events (scan modes R3-R5). From R3, the peak temperature observed in Layer 1 was below 650 K, and there was only a minor change in the microstructure, indicating the stability of the intermetallics under this heating profile. There was a good agreement between the temperature distribution determined from IR and sXRD (as shown in Figure 4(f)), confirming the precision of the results.

3.4. Stress development

The in situ sXRD enabled the experimental quantification of stress development during DED and resultant residual stress in the post-build sample. The in-plane stress components (σ_{xx} in laser scan direction (x), σ_{yy} in build direction (y), and shear stress, σ_{xy}) were calculated in the Al phase, with the assumption that the out-of-plane stress was nil for a thin wall sample[34]. As illustrated in Figure 5, σ_{yy} was the dominant stress component during deposition, with an average stress of (27.0 ± 16.6) MPa. In comparison, had an average magnitude of (10.7 ± 7.8) MPa. In addition, σ_{xy} was negligible during deposition. During DED, the melt pool induced a compressive stress field in its direct vicinity due to thermal expansion, see blue C-regions. Red T-regions, which were not adjacent to the melt pool, experienced thermal contraction and were, therefore, under tensile stress, due to the mechanical constraints from the solidified component.

The stress development during the 1st deposition layer (scan mode D1) is illustrated in Figure 5(a), with the stress formation mechanism shown schematically in Figure 5(b). The compressive stress field (blue region C1) was mainly confined to the newly solidified layer, resulting in a higher compressive stress in σ_{xx} compared to σ_{yy} in the region near the melt pool (1.2–1.6 mm from MPF). Such horizontal compressive stress partially counteracted the tensile stress in the x direction within the red region T1; therefore, the tensile stress of σ_{xx} in scan mode D1 was much lower than that of σ_{yy}.

The stress distribution of Layer 1 during 3rd layer deposition (scan mode R3) is shown in Figure 5(c), with the corresponding stress formation mechanism schematically illustrated in Figure 5(d). The compressive stress field (blue region C2) on the measured volume spreads downward, with a higher compressive stress level observed in σ_{yy}. The tensile stress regions (T2 and T3) demonstrated a higher stress level in σ_{yy} due to a higher thermal gradient in the y direction within those regions, such that the average G_y in scan mode R3 is 220.6 K·mm^{-1}, compared to G_x with 35.3 K·mm^{-1} (see Figures 4(c) and (d)). As the laser beam passed through the measured volume, the re-heating effect on the red region T2 reduced the tensile stress compared to the red region T3, which did not undergo re-heating.

Figure 5(e) shows the stress distribution of Layer 1 during the 5th layer deposition (scan mode R5) with the stress formation mechanism illustrated in Figure 5(f). In contrast to scan mode R3, there was no compressive stress field from the

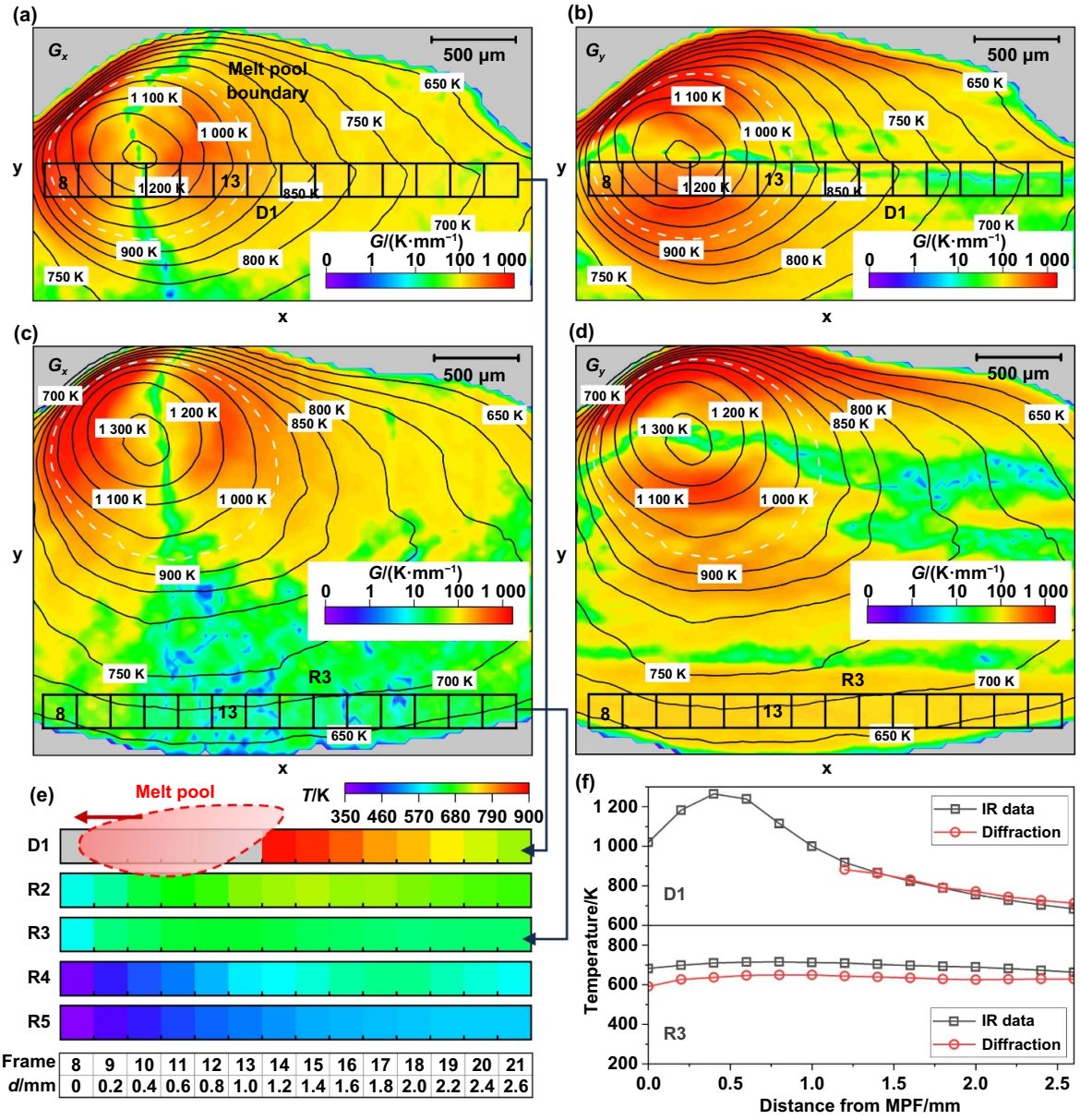

Figure 4. Temperature and thermal gradient distribution during DED PA1 aluminum (plate sample): (a) and (b) thermal gradient in x (G_x) and y (G_y) direction during deposition of Layer 1, calculated from IR temperature distribution (contour lines); (c) and (d) thermal gradient in x (G_x) and y (G_y) direction during deposition of Layer 3, calculated from IR temperature distribution (contour lines); (e) temperature distribution analyzed from diffraction data, and (f) comparison between IR and diffraction data for scan mode D1 and R3.

melt pool applied to the measured volume due to the increased distance to the laser source. The cooled region (T4) before the melt pool demonstrated tensile stress because of thermal contraction. However, the stresses of σ_{xx} and σ_{yy} in re-heated region C3 were close to the final state, and compressive stress occurred to balance the tensile stress formed in the region above.

Figure 5(g) gives the residual stress distribution of the built sample at ambient temperature, with compressive stresses of σ_{xx} and σ_{yy} observed in Layers 1 and 2, and tensile stresses observed in Layers 3 to 5. These stress (σ_{xx} and σ_{yy}) distributions agree well with reference[74–76], and can be explained through the cool-down phase mechanism[77], see Figure 5(h). During the post-deposition cooling, the shrinkage and thermal contraction of later deposited layers is constrained by the underlying layers, leading to tensile stress development in the top layers. Compressive stresses were introduced in the substrate and continued to accumulate between the bottom layers (Layers 1 and 2). The shear stresses σ_{xy} showed the opposite directions between neighboring layers due to the bi-directional scanning strategy used in DED. A previous study suggested that laser-based DED Al alloy resulted in the highest residual stress (110 MPa) of ~35% of its YS[78], while the maximum stress (130 MPa) in arc-based DED Al can even reach the YS level[79]. In comparison, the estimated residual stress (<32 MPa) in our alloy is minimal (<16% of the YS), which should lead to a lesser cracking susceptibility and shape distortion.

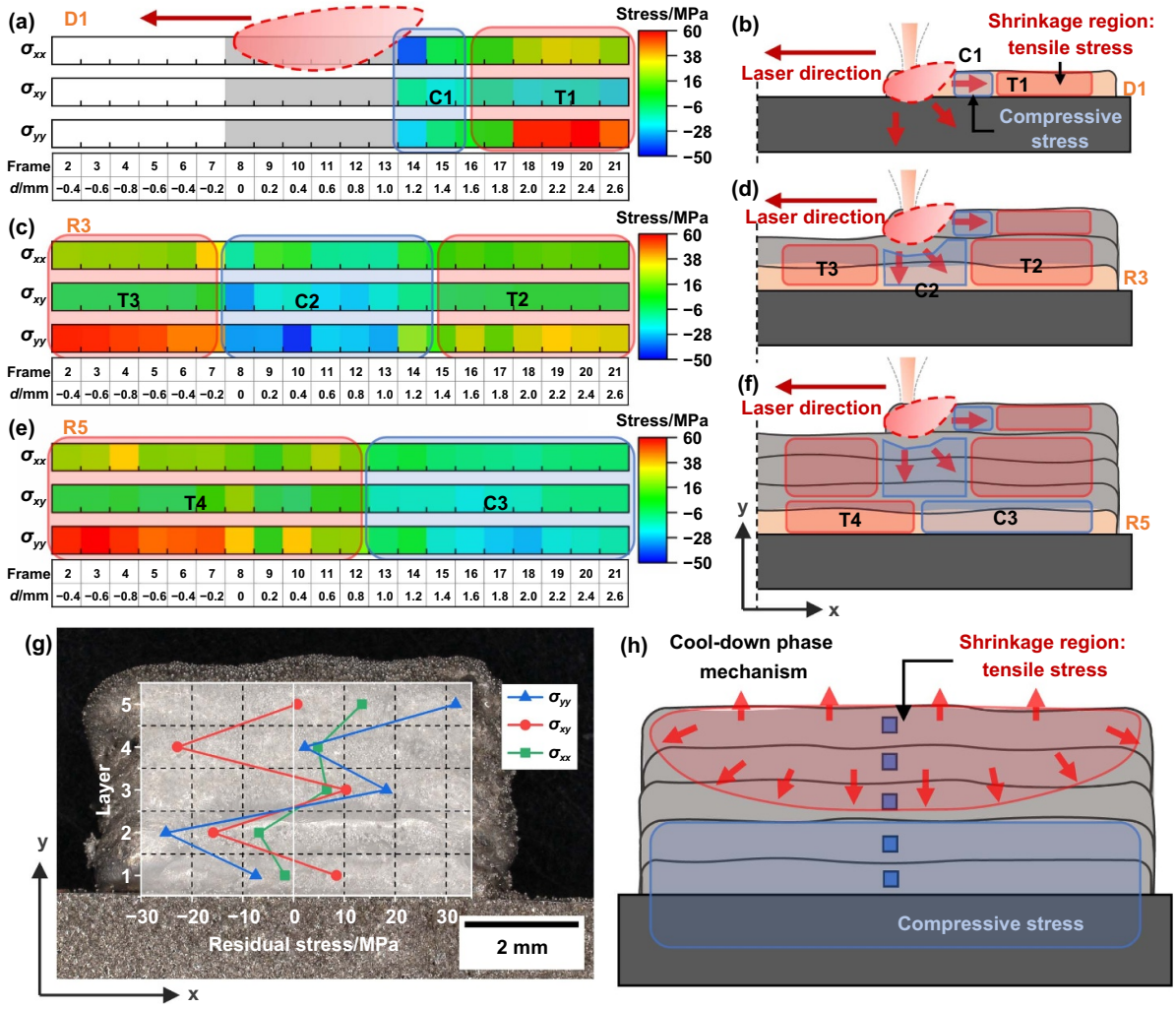

Figure 5. Stress development during DED aluminum and final residual stress: (a) in-plane stress (σ_{xx} in laser scan direction (x), σ_{yy} in build direction (y) and shear stress, σ_{xy}) development and (b) schematic of stress formation mechanism during deposition of Layer 1 (scan mode D1); (c) stress development and (d) stress formation mechanism during re-heating event of 3rd layer deposition (scan mode R3); (e) stress development and (f) stress formation mechanism during re-heating event of 5th layer deposition (R5); (g) residual stress distribution (L1 to L5) of post-build sample, and (h) schematic of cool-down phase mechanism to explain the origin of residua stress. The blue and red regions indicate the compressive and tensile regions.

Residual stress primarily arises from thermal contraction during cooling and mechanical constraints imposed by the surrounding material. During DED processing, the local in-process stress can reach 60 MPa, exceeding the final residual stress due to higher thermal gradient and rapid temperature fluctuations during DED printing. Our alloy exhibits a narrow freezing range of 2.8 °C and a linear solidification contraction of only 0.028%, which is an order of magnitude lower than that of Al 6061[80]. This substantially reduced thermal shrinkage during cooling is the principal factor responsible for the low residual stress observed in our alloy. Although sample size can also affect residual stress, leading to a low stress level, the DED-fabricated Al reported in [78] with a comparable build size shows higher values, further underscoring the advantage of our alloy.

4. Conclusion

In summary, a bespoke Al alloy based on the Al–Ni–Ce–Mn–Fe system was successfully fabricated in DED with a density over 99%, uniformly distributed intermetallics, fine sub-grain (eutectic colony) size of <5 μm, and ultra-fine eutectic lamella of ∼0.2 μm. The refined microstructure led to increases of 70% and 50% in YS and UTS, respectively, compared with those of a commonly used AM eutectic AlSi10Mg alloy. This is due to the combined effect of dispersion strengthening of the fine intermetallic formed, grain refinement strengthening, and fine lamellar strengthening. Through correlative in situ X-ray imaging, X-ray diffraction, and IR imaging, we have elucidated the mechanisms behind the structure refinement and stress formation during DED. The significantly reduced

freezing range (2.8 °C) and solidification contraction of our alloy can lead to low stress level during solidification and afterwards. This is confirmed by the experimentally estimated residual stresses that were minimal after the deposition, less than 32 MPa (<16% of yield stress) for both tensile and compressive regions. Such low residual stress should result in low cold/hot cracking susceptibility and distortion. These findings provide valuable insights into the underlying mechanisms and mechanical performance of the alloy, offering a robust framework for designing high-performance alloys that meet the stringent demands of next-generation industrial AM applications.

Data availability

Data will be made available on request.

Acknowledgments

The authors acknowledge the support from the UKRI—EPSRC, Grants Numbered EP/W006774/1, EP/P006566/1, EP/W003333/1, and EP/V061798/1. PDL is funded by the support from a Royal Academy of Engineering Chair in Emerging Technologies (CiET1819/10); CLAL is funded in part by EP/W037483/1 and IPG Photonics/ Royal Academy of Engineering Senior Research Fellowship in SEARCH (Ref: RCSRF2324-18-71). The atomization of powder was done by a proprietary ultrasonic atomization technology developed and implemented by Amazemet Sp. z o.o. This research used resources of the Diamond Light Source (DLS) in Beamline I12 (MG-34549). Many thanks to team members from the Multiscale X-ray Imaging Lab at Harwell (MXI Lab) for their assistance in preparation for and during the beamtime.

Author contributions

P.D.L., D.G.E. and I.T. and C.L.A.L. conceived the Project. D.G., K.Z., C.Z., R.W., S.M., P.D.L., and C.L.A.L. led the in situ experimental design and conducted the experiments, with all authors contributing. C.Z. and D.G.E. designed the material. D.G. led the data processing and analysis, with all authors contributing. D.G., D.G.E., C.L.A.L., P.D.L., H.E.C. and C.Z. led the results interpretation and manuscript writing, with all authors contributing. W. L. conduct the IR analysis. C.Z conduct SEM and PIP testing under D.G.E. supervision. S.B performed post CT scan.

ORCID iDs

Da Guo 0000-0003-2055-6762
Dmitry G. Eskin 0000-0002-0303-2249
Peter. D. Lee 0000-0002-3898-8881

References

[1] Gu D D, Shi X Y, Poprawe R, Bourell D L, Setchi R and Zhu J H. 2021. Material-structure-performance integrated laser-metal additive manufacturing. *Science* **372**, eabg1487.
[2] Bandyopadhyay A, Traxel K D, Lang M L N, Juhasz M, Eliaz N and Bose S. 2022. Alloy design via additive manufacturing: advantages, challenges, applications and perspectives. *Mater. Today* **52**, 207–224.
[3] Liu Z Z, Zhou Q H, Liang X K, Wang X B, Li G C, Vanmeensel K and Xie J X. 2024. Alloy design for laser powder bed fusion additive manufacturing: a critical review. *Int. J. Extrem. Manuf.* **6**, 022002.
[4] Abdali A, Hossein Nedjad S, Hamed Zargari H, Saboori A and Yildiz M. 2024. Predictive tools for the cooling rate-dependent microstructure evolution of AISI 316L stainless steel in additive manufacturing. *J. Mater. Res. Technol.* **29**, 5530–5538.
[5] Aboulkhair N T, Everitt N M, Ashcroft I and Tuck C. 2014. Reducing porosity in AlSi10Mg parts processed by selective laser melting. *Addit. Manuf.* **1–4**, 77–86.
[6] Eskin D G et al. 2004. Mechanical properties in the semi-solid state and hot tearing of aluminium alloys. *Prog. Mater. Sci.* **49**, 629–711.
[7] Michi R A, Plotkowski A, Shyam A, Dehoff R R and Babu S S. 2022. Towards high-temperature applications of aluminium alloys enabled by additive manufacturing. *Int. Mater. Rev.* **67**, 298–345.
[8] Shang A Y et al. 2024. Additive manufacturing of an ultrastrong, deformable Al alloy with nanoscale intermetallics. *Nat. Commun.* **15**, 5122.
[9] Spierings A B, Dawson K, Kern K, Palm F and Wegener K. 2017. SLM-processed Sc- and Zr- modified Al-Mg alloy: mechanical properties and microstructural effects of heat treatment. *Mater. Sci. Eng. A* **701**, 264–273.
[10] Pauzon C, Buttard M, Després A, Charlot F, Fivel M, Chehab B, Blandin J-J and Martin G. 2023. Direct ageing of LPBF Al-1Fe-1Zr for high conductivity and mechanical performance. *Acta Mater.* **258**, 119199.
[11] Guo D, Lambert-Garcia R, Hocine S, Fan X Q, Greenhalgh H, Shahani R, Majkut M, Rack A, Lee P D and Alex Leung C L. 2024. Correlative spatter and vapour depression dynamics during laser powder bed fusion of an Al-Fe-Zr alloy. *Int. J. Extrem. Manuf.* **6**, 055601.
[12] Martin J H, Yahata B D, Hundley J M, Mayer J A, Schaedler T A and Pollock T M. 2017. 3D printing of high-strength aluminium alloys. *Nature* **549**, 365–369.
[13] Dan C Y et al. 2023. Achieving ultrahigh fatigue resistance in AlSi10Mg alloy by additive manufacturing. *Nat. Mater.* **22**, 1182–1188.
[14] Sui S, Chew Y, Weng F, Tan C L, Du Z L and Bi G J. 2022. Study of the intrinsic mechanisms of nickel additive for grain refinement and strength enhancement of laser aided additively manufactured Ti–6Al–4V. *Int. J. Extrem. Manuf.* **4**, 035102.
[15] Wang W Y, Takata N, Suzuki A, Kobashi M and Kato M. 2023. Design of Al–Fe–Mn alloy for both high-temperature strength and sufficient processability of laser powder bed fusion. *Addit. Manuf.* **68**, 103524.
[16] Wu T, Poplawsky J D, Allard L F, Plotkowski A, Shyam A and Dunand D C. 2023. Microstructure and strengthening of Al-6Ce-3Ni-0.7Fe (wt%) alloy manufactured by laser powder-bed fusion. *Addit. Manuf.* **78**, 103858.
[17] Michi R A, Sisco K, Bahl S, Yang Y, Poplawsky J D, Allard L F, Dehoff R R, Plotkowski A and Shyam A. 2022. A creep-resistant additively manufactured Al-Ce-Ni-Mn alloy. *Acta Mater.* **227**, 117699.
[18] Leung C L A, Marussi S, Atwood R C, Towrie M, Withers P J and Lee P D. 2018. In situ X-ray imaging of defect and molten pool dynamics in laser additive manufacturing. *Nat. Commun.* **9**, 1355.
[19] Zhang K et al. 2024. Pore evolution mechanisms during directed energy deposition additive manufacturing. *Nat. Commun.* **15**, 1715.

[20] Fan X Q, Fleming T G, Clark S J, Fezzaa K, Getley A C M, Marussi S, Wang H Z, Leung C L A, Kao A and Lee P D. 2025. Magnetic modulation of keyhole instability during laser welding and additive manufacturing. *Science* **387**, 864–869.
[21] Lin J-F, Degtyareva O, Prewitt C T, Dera P, Sata N, Gregoryanz E, Mao H-K and Hemley R J. 2024. Crystal structure of a high-pressure/high-temperature phase of alumina by in situ X-ray diffraction. *Nat. Mater.* **3**, 389–393.
[22] Zhang D S, Liu W, Li Y X, Sun D R, Wu Y, Luo S N, Chen S, Tao Y and Zhang B B. 2023. In situ observation of crystal rotation in Ni-based superalloy during additive manufacturing process. *Nat. Commun.* **14**, 2961.
[23] Hocine S, Van Swygenhoven H, Van Petegem S, Chang C S T, Maimaitiyili T, Tinti G, Ferreira Sanchez D, Grolimund D and Casati N. 2020. Operando X-ray diffraction during laser 3D printing. *Mater. Today* **34**, 30–40.
[24] Lifshitz I M and Slyozov V V. 1961. The kinetics of precipitation from supersaturated solid solutions. *J. Phys. Chem. Solids* **19**, 35–50.
[25] Czerwinski F. 2020. Cerium in aluminum alloys. *J. Mater. Sci.* **55**, 24–72.
[26] Plotkowski A, Sisco K, Bahl S, Shyam A, Yang Y, Allard L, Nandwana P, Rossy A M and Dehoff R R. 2020. Microstructure and properties of a high temperature Al–Ce–Mn alloy produced by additive manufacturing. *Acta Mater.* **196**, 595–608.
[27] Cowley I et al. 2026. A second-generation apparatus for in situ synchrotron characterisation of directed energy deposition additive manufacturing with multi-modal monitoring and external forces. *Mater. Des.* **262**, 115495.
[28] Drakopoulos M et al. 2015. I12: the joint engineering, environment and processing (JEEP) beamline at diamond light source. *J. Synchrotron Radiat.* **22**, 828–838.
[29] Wen C-D and Mudawar I. 2004. Emissivity characteristics of roughened aluminum alloy surfaces and assessment of multispectral radiation thermometry (MRT) emissivity models. *Int. J. Heat Mass Transfer* **47**, 3591–3605.
[30] Zhang K H, Yu K, Liu Y F and Zhao Y J. 2017. Effect of surface oxidation on emissivity properties of pure aluminum in the near infrared region. *Mater. Res. Express* **4**, 086501.
[31] Basham M et al. 2015. Data analysis WorkbeNch (DAWN). *J. Synchrotron Radiat.* **22**, 853–858.
[32] Filik J et al. 2017. Processing two-dimensional X-ray diffraction and small-angle scattering data in DAWN 2. *J. Appl. Crystallogr.* **50**, 959–966.
[33] Brückner S. 2000. Estimation of the background in powder diffraction patterns through a robust smoothing procedure. *J. Appl. Crystallogr.* **33**, 977–979.
[34] Chen Y H et al. 2021. Correlative synchrotron X-ray imaging and diffraction of directed energy deposition additive manufacturing. *Acta Mater.* **209**, 116777.
[35] Collins D M, Crudden D J, Alabort E, Connolley T and Reed R C. 2015. Time-resolved synchrotron diffractometry of phase transformations in high strength nickel-based superalloys. *Acta Mater.* **94**, 244–256.
[36] Prince E and Boggs P T. 2006. Least squares. *In International Tables for Crystallography, Volume C* (ed Prince E) (Springer) pp 678–688.
[37] Boucherle J X, Givord F, Lapertot G, Muñoz A and Schweizer J. 1995. The magnetic structures of Ce3Al11: a single crystal study. *J. Magn. Magn. Mater.* **148**, 397–408.
[38] Gout D, Benbow E, Gourdon O and Miller G J. 2003. Crystallographic, electronic and magnetic studies of Ce4Ni6Al23: a new ternary intermetallic compound in the cerium–nickel–aluminum phase diagram. *J. Solid State Chem.* **174**, 471–481.
[39] Kangas M J, Schmitt D C, Sakai A, Nakatsuji S and Chan J Y. 2012. Structure and physical properties of single crystal PrCr2Al20 and CeM2Al20 (M=V, Cr): a comparison of compounds adopting the CeCr2Al20 structure type. *J. Solid State Chem.* **196**, 274–281.
[40] Chumak I, Richter K W and Ipser H. 2007. The Fe–Ni–Al phase diagram in the Al-rich (>50at.% Al) corner. *Intermetallics* **15**, 1416–1424.
[41] Li C, Zhang X, Chen Y, Carr J, Jacques S, Behnsen J, Di Michiel M, Xiao P and Cernik R. 2017. Understanding the residual stress distribution through the thickness of atmosphere plasma sprayed (APS) thermal barrier coatings (TBCs) by high energy synchrotron XRD; digital image correlation (DIC) and image based modelling. *Acta Mater.* **132**, 1–12.
[42] Wang T, Zhu J Z, Chen L Q, Liu Z-K and Mackay R A. 2004. Modeling of lattice parameter in the Ni-Al system. *Metall. Mater. Trans. A* **35**, 2313–2321.
[43] Welzel U, Ligot J, Lamparter P, Vermeulen A and Mittemeijer E. 2005. Stress analysis of polycrystalline thin films and surface regions by X-ray diffraction. *J. Appl. Crystallogr.* **38**, 1–29.
[44] Sparks T, Kuksenko V, Gorley M, Hoffmann J, Chiu Y-L, Connolley T, Rieth M, Wang Y Q and Cai B. 2024. In-Situ synchrotron investigation of elastic and tensile properties of oxide dispersion strengthened EUROFER97 steel for advanced fusion reactors. *Acta Mater.* **271**, 119876.
[45] Sutton P M. 1953. The variation of the elastic constants of crystalline aluminum with temperature between 63°K and 773°K. *Phys. Rev.* **91**, 816–821.
[46] Gu W C, Campbell J, Tang Y B, Safaie H, Johnston R, Gu Y C, Pleydell-Pearce C, Burley M, Dean J and Clyne T W. 2022. Indentation plastometry of welds. *Adv. Eng. Mater.* **24**, 2101645.
[47] Southern T J F, Campbell J E, Fang C, Nemcova A, Bannister A and Clyne T W. 2023. Use of hardness, PIP and tensile testing to obtain stress-strain relationships for metals. *Mech. Mater.* **187**, 104846.
[48] Tang Y T, Campbell J E, Burley M, Dean J, Reed R and Clyne T W. 2021. Profilometry-based indentation plastometry to obtain stress-strain curves from anisotropic superalloy components made by additive manufacturing. *Materialia* **15**, 101017.
[49] Southern T, Campbell J E, Kourousis K I, Mooney B, Tang Y T and Clyne T W. 2023. Indentation plastometry for study of anisotropy and inhomogeneity in maraging steel produced by laser powder bed fusion. *Steel Res. Int.* **94**, 2200881.
[50] Xu H, Ren W J, Ma C Y, Xu L Y, Han Y D, Zhao L and Hao K D. 2023. Laser-directed energy deposition of ZrH2 particles reinforced Al7075 alloy: cracks elimination and strength enhancement. *Addit. Manuf.* **78**, 103877.
[51] Gong J Q, Wei K W, Liu M N, Song W J, Li X Y and Zeng X Y. 2022. Microstructure and mechanical properties of AlSi10Mg alloy built by laser powder bed fusion/direct energy deposition hybrid laser additive manufacturing. *Addit. Manuf.* **59**, 103160.
[52] Gu T, Chen B, Tan C W and Feng J C. 2019. Microstructure evolution and mechanical properties of laser additive manufacturing of high strength Al-Cu-Mg alloy. *Opt. Laser Technol.* **112**, 140–150.
[53] Zhang W, Ha K, Jin Q Y, Nam H, Park J and Lee W. 2023. Effects of laser rescanning on microstructure and mechanical properties of Al-10Si-1Mg alloy produced by laser-directed energy deposition. *Mater. Today Commun.* **37**, 106979.
[54] Lv F, Shen L D, Liang H X, Xie D Q, Wang C J and Tian Z J. 2019. Mechanical properties of AlSi10Mg alloy fabricated by laser melting deposition and improvements via heat treatment. *Optik* **179**, 8–18.
[55] Wang X, Li L Q, Qu J Y and Tao W. 2019. Microstructure and mechanical properties of laser metal deposited AlSi10Mg alloys. *Mater. Sci. Technol.* **35**, 2284–2293.

[56] Su Y T, Wang Y C and Shi J. 2022. Microstructure and mechanical properties of laser DED produced crack-free Al 7075 alloy: effect of process parameters and heat treatment. *Mater. Sci. Eng. A* **857**, 144075.
[57] Balla S K, Mallaiah M, Nagamuthu S, Gurugubelli R C, Aranas C and Bontha S. 2024. The influence of laser direct energy deposition processing parameters on Al7075 alloy and Zr-modified Al7075 alloy. *Int. J. Adv. Manuf. Technol.* **135**, 181–201.
[58] Su Y T, Savinov R, Wang Y C, Lin D and Shi J. 2024. Microstructure and property enhancement of 7075 aluminium alloy via laser metal deposition augmented by in-situ ultrasonic vibration. *Virtual Phys. Prototyp.* **19**, e2301482.
[59] Deng C, Li R D, Yuan T C, Niu P D and Wang Y. 2024. Microstructure and mechanical properties of a combination interface between direct energy deposition and selective laser melted Al-Mg-Sc-Zr alloy. *Metals* **11**, 801.
[60] Xu R, Li R D, Yuan T C, Zhu H B and Li P. 2022. Microstructure and mechanical properties of TiC-reinforced Al–Mg–Sc–Zr composites additively manufactured by laser direct energy deposition. *Acta Metall. Sin.* **35**, 411–424.
[61] Wang Q Z et al. 2022. Effect of laser additive manufacturing on the microstructure and mechanical properties of TiB2 reinforced Al-Cu matrix composite. *Mater. Sci. Eng. A* **840**, 142950.
[62] Ding F, Fu A, Wang J, Xie Z H, Cao Y K, Li J, Fang Q H and Liu B. 2023. Significant strength enhancement of FeCrNiMox medium-entropy alloys via hard intermetallic particles dispersion strengthening. *Mater. Charact.* **200**, 112877.
[63] Ekaputra C N, Mogonye J E and Dunand D C. 2025. Evolution of eutectic microstructure and strength in an Al-Ce-Ni-Mn-Sc-Zr alloy fabricated by laser powder-bed fusion. *Addit. Manuf.* **109**, 104903.
[64] Liu W H, Lu Z P, He J Y, Luan J H, Wang Z J, Liu B, Liu Y, Chen M W and Liu C T. 2016. Ductile CoCrFeNiMox high entropy alloys strengthened by hard intermetallic phases. *Acta Mater.* **116**, 332–342.
[65] Ekaputra C N, Mogonye J-E and Dunand D C. 2024. Microstructure and mechanical properties of cast, eutectic Al-Ce-Ni-Mn-Sc-Zr alloys with multiple strengthening mechanisms. *Acta Mater.* **274**, 120006.
[66] Sims Z C, Weiss D, McCall S K, McGuire M A, Ott R T, Geer T, Rios O and Turchi P A E. 2016. Cerium-based, intermetallic-strengthened aluminum casting alloy: high-volume co-product development. *JOM* **68**, 1940–1947.
[67] Yang Y, Bahl S, Sisco K, Lance M, Shin D, Shyam A, Plotkowski A and Dehoff R R. 2020. Primary solidification of ternary compounds in Al-rich Al–Ce–Mn alloys. *J. Alloy Compd.* **844**, 156048.
[68] Kozakevich J R, Stroh J, Sediako D and Weiss D. 2023. Solidification kinetics of an Al-Ce alloy with additions of Ni and Mn. *Metals* **13**, 955.
[69] Ekaputra C N, Rakhmonov J U, Senvardarli E, Weiss D, Mogonye J E and Dunand D C. 2024. Design and characterization of hierarchically-strengthened, cast Al-Ce-Ni-Mn-Sc-Zr alloys for high-temperature applications. *In Light Metals 2024* (ed Wagstaff S) (Springer)
[70] Raghavan N, Dehoff R, Pannala S, Simunovic S, Kirka M, Turner J, Carlson N and Babu S S. 2016. Numerical modeling of heat-transfer and the influence of process parameters on tailoring the grain morphology of IN718 in electron beam additive manufacturing. *Acta Mater.* **112**, 303–314.
[71] Parry L, Ashcroft I A and Wildman R D. 2016. Understanding the effect of laser scan strategy on residual stress in selective laser melting through thermo-mechanical simulation. *Addit. Manuf.* **12**, 1–15.
[72] Hagenlocher C, O'toole P, Xu W, Brandt M, Easton M and Molotnikov A. 2022. In process monitoring of the thermal profile during solidification in laser directed energy deposition of aluminium. *Addit. Manuf. Lett.* **3**, 100084.
[73] Shi S Q, Lin X, Wang L L, Wang Z N, Wei L, Yang H O, Tang Y and Huang W D. 2023. Investigations of the processing–structure–performance relationships of an additively manufactured AlSi10Mg alloy via directed energy deposition. *J. Alloy Compd.* **944**, 169050.
[74] Levkulich N C, Semiatin S L, Gockel J E, Middendorf J R, Dewald A T and Klingbeil N W. 2019. The effect of process parameters on residual stress evolution and distortion in the laser powder bed fusion of Ti-6Al-4V. *Addit. Manuf.* **28**, 475–484.
[75] Jeong S G, Ahn S Y, Kim E S, Karthik G M, Baik Y, Seong D, Kim Y S, Woo W and Kim H S. 2022. Effect of substrate yield strength and grain size on the residual stress of direct energy deposition additive manufacturing measured by neutron diffraction. *Mater. Sci. Eng. A* **851**, 143632.
[76] Guo D, Yan K, Callaghan M D, Daisenberger D, Chatterton M, Chen J D, Wisbey A and Mirihanage W. 2021. Solidification microstructure and residual stress correlations in direct energy deposited type 316L stainless steel. *Mater. Des.* **207**, 109782.
[77] Mercelis P and Kruth J-P. 2006. Residual stresses in selective laser sintering and selective laser melting. *Rapid Prototyp. J.* **12**, 254–265.
[78] Caiazzo F, Alfieri V and Bolelli G. 2022. Residual stress in laser-based directed energy deposition of aluminum alloy 2024: simulation and validation. *Int. J. Adv. Manuf. Technol.* **118**, 1197–1211.
[79] Hönnige J R, Colegrove P A, Ganguly S, Eimer E, Kabra S and Williams S. 2018. Control of residual stress and distortion in aluminium wire + arc additive manufacture with rolling. *Addit. Manuf.* **22**, 775–783.
[80] Zhu C B, Guo D, Leung C L A, Tzanakis I, Lee P D and Eskin D. 2025. Design of hot-tearing resistant and thermally stable aluminium alloys for advanced casting technologies. *Mater. Des.* **260**, 115152.